



Structural, optical and enhanced multiferroic properties of La/Cr co-substituted BiFeO₃ nanostructures

M. Nadeem¹ · Wasi Khan² · Shakeel Khan¹ · Shahid Husain² · Fouran Singh³ · Azizurrahman Ansari² · D. K. Shukla⁴ · Abdul Ahad² · Vishal Kumar Chakradhary⁵ · M. J. Akhtar⁵

Received: 29 February 2020 / Revised: 20 May 2020 / Accepted: 22 May 2020 / Published online: 1 June 2020
© Springer Science+Business Media, LLC, part of Springer Nature 2020

Abstract

We have synthesized BiFeO₃ (BFO) and Bi_{0.5}La_{0.5}Fe_{1-x}Cr_xO₃ ($0 \leq x \leq 0.06$) samples via sol–gel process with the objective to explore the influence of La/Cr co-doping on the structural, optical, dielectric and multiferroic properties of BFO. Rietveld refinement analysis and Raman active modes affirm single-phase and rhombohedral crystal structure of the samples in $R3c$ space group. The UV–visible-DRS data reveal a systematic reduction of the bandgap and increase in the Urbach energy (E_u) with the increase of La/Cr content in BFO matrix. The temperature-dependent dielectric measurements divulge that the BFO has the highest dielectric constant, and relaxation peak shifts with the rise in frequency that proposes the possibility of the thermally activated relaxation mechanism which also supported through the Vogel–Fulcher model. The magnetic hysteresis ($M-H$) loops exhibit ferromagnetic nature of all the samples at room temperature except BFO. The $P-E$ hysteresis loops display ferroelectric behavior with higher values of polarization and coercive field in the doped samples.

1 Introduction

The extraordinary class of materials that shows more than one ferroic nature is termed as multiferroics [1, 2]. During the last couple of decades, significant attention has been paid by the researchers to these materials because of the conjunction of more than one ferroic or anti-ferroic properties, i.e., ferroelectric, ferromagnetic as well as ferroelastic in the single-phase [3, 4]. Besides this, the fundamental physics of these materials is likewise fascinating. Multiferroics are very important for the technological applications point of view because of the coupling between the ferro-phases

and the piezo-elastic properties. These highlights make them a reasonable competitor for their potential applications in spintronics, information technology, transducers, sensors, actuators and data storage media [5–7]. The simultaneous existence of ferroelectricity with ferromagnetism is an interesting speculate since the requirement of empty d orbitals for ferroelectricity is not suitable with confined transition metal d electrons for magnetism [8]. The presence of localized electrons, typically in the partially filled d shells of transition-metal is the origin of magnetism, which has a corresponding magnetic moment or localized spin. The exchange interactions among the localized moments give rise to magnetic ordering. The circumstances with ferroelectrics are relatively dissimilar. However, there are various causes of ferroelectricity, and likewise, one can have different kinds of multiferroics. In type-I multiferroics, the critical temperature of the ferroelectric and magnetic transitions are predominantly above room temperature, and the spontaneous polarization is frequently somewhat huge, i.e., ~ 10 to $100 \mu\text{C}/\text{cm}^2$ [2, 9, 10].

Among few promising multiferroics, perovskite (ABO₃) based bismuth ferrite BiFeO₃ (BFO) is the most familiar room-temperature multiferroic material with rhombohedral distorted perovskite structure having $R3c$ space group, and the presence of coexisting ferroic orders combined with (anti)ferroelectricity, (anti)ferromagnetism and

✉ Wasi Khan
wasiamu@gmail.com

¹ Department of Applied Physics, Z.H. College of Engineering & Technology, Aligarh Muslim University, Aligarh 202002, India

² Department of Physics, Aligarh Muslim University, Aligarh 202002, India

³ Inter-University Accelerator Centre, Aruna Asaf Ali Marg, New Delhi 110067, India

⁴ UGC-DAE Consortium for Scientific Research, Khandwa Road, Indore 452017, India

⁵ Materials Science Programme, Indian Institute of Technology Kanpur, Kanpur 208016, India

ferroelasticity [11, 12]. Moreover, the BFO is a fantastic multiferroic material owing to its vast polarization (i.e., $100 \mu\text{C}/\text{cm}^2$) and high ferroelectric Curie temperature ($T_C \sim 1103 \text{ K}$). From the magnetic perspective, the BFO is a G-type antiferromagnet below the Néel temperature ($T_N \sim 643 \text{ K}$) [13, 14]. The bulk BFO shows antiferromagnetic behavior from the prompt effect of the spiral spin structure with a period of $\sim 620 \text{ \AA}$ [15]. This material is presently the subject of rigorous investigations since it opened the way to absolutely new applications for multiple-state memories, data storage systems, high-energy density capacitors, memory devices, nonlinear optics, satellite communications, sensors, photoelectrochemical cells, optical filters, photocatalysis, magnetically controlled piezoelectric transducers, electric field-controlled ferromagnetic resonance devices and so on [16, 17]. Apart from its intense multiferroic behavior, it has few obstacles such as single-phase synthesis, weak magneto-electric coupling, the small value of magnetization, large leakage current, and low remanent polarization. Many researchers have established different strategies to prepare nanostructures of various sizes and shapes that straightforwardly influence the various properties of the system. Still, the preparation of monophasic BFO is problematic by means of the ordinary solid-state reaction route as a result of the volatile nature of bismuth and the occurrence of the secondary phases, e.g., $\text{Bi}_{25}\text{FeO}_{40}$ and $\text{Bi}_2\text{Fe}_4\text{O}_9$ that are unescapable at high-temperature environments [18]. Remarkably, the sol-gel process provides considerable better outcomes to acquire the BFO in monophasic as it is a low-temperature process that keeps control of the loss of Bi [11]. However, the large leakage current is an obstruction in the process of using this material in real applications. In addition, co-doping of multi-elements at A and B sites, in order to improve ferroelectric nature, magneto-electric coupling and to reduce the leakage current are under investigations [19, 20]. Additionally, the high conductivity of BFO is an outcome of the occurrence of oxygen vacancies and Fe^{2+} ions that makes it incredibly hard to perceive the ferroelectric hysteresis loop. These issues also affect the magnetic nature of BFO. The particle size below the periodicity reveals destruction of the antiferromagnetically ordered spin cycloid. This incites scientists to decrease the particle size to enhance magnetization [21].

The improvement in the dielectric and magnetic properties, along with the reduction in dielectric loss has been observed by Mishra et al. [22] and Gautam et al. [23] in the yttrium doped BFO system. Singh et al. [4] have described that co-doping in BFO could satisfactorily increase the polarization in view of the alteration in the bond angle of Fe–O–Fe related to the bending emerges because of dopant ions. It has been noticed in the La-doped BFO system that the ferromagnetic properties have been enhanced, and reduction of the leakage current density gives rise to the

polarization hysteresis loop [24]. It also has been observed that the co-doping of multielement at Bi and Fe sites of BFO is an effective way to reduce the leakage current density and to enhance the magnetization [25, 26]. Uniyal et al. [27] have studied the Pr doped BFO multiferroic and reported an increase in the resistivity that significantly enhances the electrical polarization. The leakage current density has reduced to $10^{-7} \text{ A}/\text{cm}^2$ for Yb doped BFO and thereby enhance ferroelectric nature and dielectric properties as well [28]. The reduction of the leakage current density is attributed to the suppression of oxygen vacancies. It has been observed that the holmium (Ho) ions are effective in enhancing the magnetic properties of BiFeO_3 . This may be associated with the highest magnetic moment of Ho (i.e., $10.6 \mu_B$) among all the rare earth ions [29]. However, Mukherjee et al. [30] have observed the enhance magnetic, electrical, and magnetodielectric properties in nanocrystalline Sm-doped BFO. Besides the multiferroic nature, BiFeO_3 is an outstanding photocatalyst because of its small bandgap. In this context, various scientists have reported improved photocatalytic performance of doped BFO [31–33]. It has been reported that the doping of La at Bi site of BFO may easily produce lattice distortion because of the smaller ionic radii of La compared to Bi. This will change the canting angle between FeO_6 octahedral in neighbouring unit cells that may suppress cycloid spin structure and finally improve the magnetization. In addition, La doping in BFO has been found extensively effective from various aspects such as single-phase synthesis, improved magnetization, reduced leakage current density and enhanced multiferroic nature [4, 11, 24].

In the present study, we have simultaneously doped La^{3+} (with a fixed content 0.5) and Cr^{3+} ions into A and B sites of BiFeO_3 , respectively. The enhancement in the dielectric and multiferroic properties is observed in the La/Cr co-doped samples as compared to the pristine BiFeO_3 nanostructures.

2 Experimental detail

The cost-effective ethylene glycol-based sol-gel process is used to synthesize BiFeO_3 and $\text{Bi}_{0.5}\text{La}_{0.5}\text{Fe}_{1-x}\text{Cr}_x\text{O}_3$ ($x = 0, 0.02, 0.04$ and 0.06) nanoparticles [33]. In this process, stoichiometric amounts of AR grade $\text{Bi}(\text{NO}_3)_3 \cdot 5\text{H}_2\text{O}$, $\text{La}(\text{NO}_3)_3 \cdot 6\text{H}_2\text{O}$, $\text{Fe}(\text{NO}_3)_3 \cdot 9\text{H}_2\text{O}$, and $\text{Cr}(\text{NO}_3)_3 \cdot 9\text{H}_2\text{O}$ were mixed in diluted nitric acid and ethylene glycol. The mixture of the precursors was stirred for 1 h on a magnetic stirrer to get the homogeneous solution, and NaOH was mixed dropwise to maintain its pH value 10. After that, the continuous stirring of the solution was done for 5 h by keeping its temperature $50\text{--}60 \text{ }^\circ\text{C}$. The precipitate was washed several times with distilled water and ethanol to obtain the desired material. Subsequently, the material was dried for 24 h at $100 \text{ }^\circ\text{C}$ in an oven and then

ground in powder form. At last, the prepared samples were sintered for 6 h at 600 °C. In this way, a series of BiFeO₃ and Bi_{0.5}La_{0.5}Fe_{1-x}Cr_xO₃ ($x = 0, 0.02, 0.04, \text{ and } 0.06$) samples, named as BFO, BLFO, BLFCO2, BLFCO4, and BLFCO6 respectively were prepared. The various techniques, such as x-ray diffraction (XRD), Raman scattering, Fourier transform infrared (FTIR) spectroscopy, vibrating sample magnetometer (VSM), UV–visible diffuse reflectance spectroscopy (DRS), LCR meter and P – E loop tracer were used to characterize the samples. XRD patterns were obtained through Shimadzu LabX 6100 diffractometer with Cu K α ($\lambda = 1.5406 \text{ \AA}$) source in the 2θ range of 20–80° in order to confirm crystal structure and phase purity of the samples. FullProf Suite software has been used for the Rietveld refinement analysis of the XRD data. The room temperature Raman spectra of the samples were recorded in the wavenumber range of 50–650 cm⁻¹ using a Horiba JY HR800 micro-Raman system. The FTIR spectra were registered in the wavenumber range of 400–4000 cm⁻¹ by PerkinElmer spectrum-2 spectrometer. UV–visible DRS spectra were acquired with the PerkinElmer Lambda-950 UV–Vis–NIR spectrometer in the wavelength range of 350–700 nm. The field-dependent magnetization (M – H) loops were observed through VSM at room temperature. Temperature-dependent dielectric measurements have been performed using HIOKI 3536 LCR meter and Cryocon temperature controller in the frequency and temperature range of 4 Hz to 1 MHz and 100–500 K, respectively. The polarization versus electric field (P – E) hysteresis loops of the samples were observed using Standard Multiferroic PE Loop Ferroelectric Test System (Marine India, Model: 20PME 1 kHz 0.01M) at room temperature.

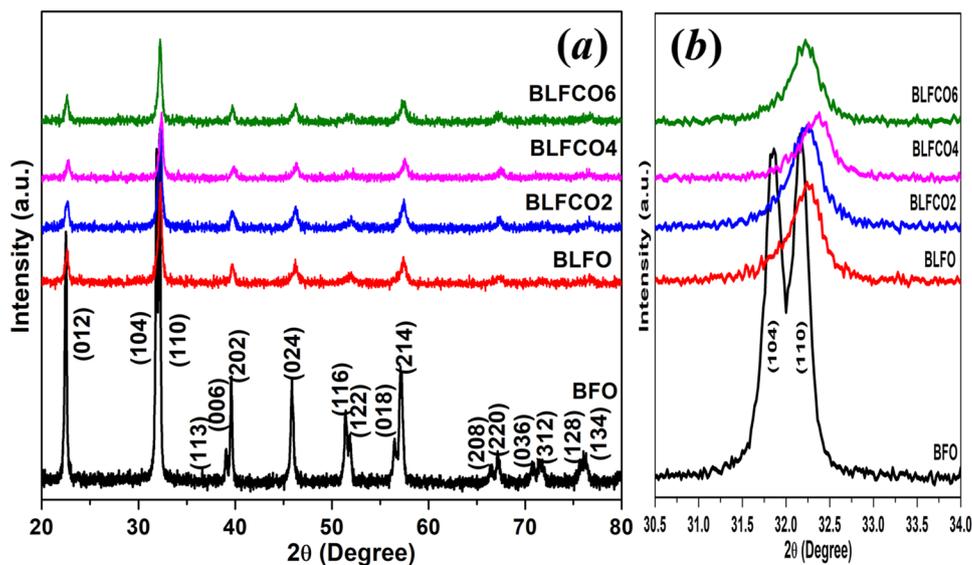
3 Results and discussion

3.1 Structural analysis

3.1.1 X-ray diffraction

In order to explore the influence of the La/Cr co-doping on the crystal structure of BFO, the XRD measurements were performed at room temperature. The XRD patterns of BFO, BLFO, BLFCO2, BLFCO4, and BLFCO6 samples are presented in Fig. 1a. All the observed diffraction peaks were assigned to the $R3c$ space group of rhombohedral structure and well-matched with previous reports (JCPDS File No. 71-2494) [34]. It is quite clear from the XRD patterns that all the samples are in single-phase, and no other peaks of secondary/impurity phase are detected in the samples. The XRD pattern of BFO exhibits two most intense diffraction peaks (104) and (110) at around $2\theta \sim 31.9$ and 32.2° which are clearly separated and intend to merge into a single peak for co-doped samples. The partial merging of these two peaks may be due to the structural distortion produced by the doping of La and Cr having lower ionic radii than the Bi and Fe respectively. The intensity of these two peaks reduces in the doped samples, as evident from Fig. 1b. Moreover, the (104)/(110) peaks shift towards the higher diffraction angle up to 4% Cr doped sample, but further doping shifts its position towards the lower angle. The average crystallite size (δ) of all the samples is evaluated from the most intense (110) peak using the Scherrer's equation, $\delta = 0.9\lambda/\beta\cos\theta$ (here λ , θ and β are the wavelength of X-rays, peak position, and FWHM, respectively) [33]. The increase in the crystallite sizes is noticed with the increase in La/Cr concentration up to 4% Cr, and further doping decreases its value.

Fig. 1 a XRD patterns and b magnified view of (104) and (110) diffraction peaks of BFO, BLFO, BLFCO2, BLFCO4 and BLFCO6 samples



This increase in the crystallite size may be ascribed to the mismatch of the effective ionic radii of Bi^{3+} (1.17 Å) and La^{3+} (1.16 Å) and similarly for Fe^{3+} (0.645 Å) and Cr^{3+} (0.615 Å) ions or due to strain-induced on doping [35]. It is quite clear from Table 1 that the lattice parameters and unit cell volume decrease with the increase in the amount of La/Cr content up to 4% of Cr doping. The estimated values of average crystallite size are found to be 15, 17, 19, 22, and 20 nm for BFO, BLFO, BLFCO2, BLFCO4, and BLFCO6 samples, respectively. Furthermore, the structural stability of the BFO and co-doped BFO have been evaluated by the Goldschmidt tolerance factor (τ) that gives the degree of distortion for the perovskites through the expression, $\tau = (r_{\text{Bi}} + r_{\text{O}})/\sqrt{2}(r_{\text{Fe}} + r_{\text{O}})$, here r is the ionic radius of the respective element [36]. For the ideal perovskite structure, the value of $\tau = 1$ and the angle of oxygen octahedron tilting is zero, whereas $\tau < 1$ specifies a compressive strain associated with the lattice mismatch amid cations. The deviation in the values of τ signifies more structural distortion. In this study, the evaluated values of the tolerance factor are 0.8886, 0.8869, 0.8872, 0.8874, and 0.8877 of the BFO, BLFO, BLFCO2, BLFCO4 and BLFCO6 samples, respectively, that advocate the slight deviation and distortion of BiFeO_3 structure on increasing Cr content. The influence of La/Cr co-doping on the crystal structure of BiFeO_3 nanoparticles is likewise investigated through Rietveld refinement of the XRD data and the refined patterns are presented in Fig. 2. It is evident that no structural transformation is observed on the doping of La/Cr ions in BFO. The experimental profiles have been fitted with the most appropriate Thompson–Cox–Hastings pseudo–Voigt function. For $K_{\alpha 1}$ and $K_{\alpha 2}$ both the profiles, line broadening function $B(2\theta)$ may be given as the pseudo–Voigt function:

$$pV(x) = \eta L(x) + (1 - \eta)G(x) \quad (1)$$

Here, $G(x)$ and $L(x)$ are the Gaussian and Lorentzian components, respectively.

The integrated intensity of the peaks has been considered as a function of structural parameters. To minimize the difference between the simulated and observed patterns, the Marquardt least-squares method has been implemented. The background has been assessed by the method of direct inclusion among selected background points. The minimization has been done by the reliability index parameter like the residuals for the weighted pattern R_{wp} , the pattern R_{p} , Bragg's factor R_{Bragg} , structure factor R_{F} , and goodness of fit χ^2 .

$$\chi^2 = [R_{\text{wp}}/R_{\text{exp}}]^2 \quad (2)$$

The goodness of fit (GOF) is esteemed by linking R_{wp} with the expected error R_{exp} . This prompts the estimation of the GOF:

$$\text{GOF} = R_{\text{wp}}/R_{\text{exp}} \quad (3)$$

Refinements have been done until the convergence was reached, and the observed value of the GOF factor tends closer to 1. The profile fitting technique was changed in accordance with the limit of χ^2 function [37]. The obtained structural parameters, Fe–O–Fe bond angles, and Fe–O bond lengths from the Rietveld refinement are tabulated in Table 1.

3.1.2 Raman spectroscopy

Raman measurements have been performed to explore the doping effects of $\text{La}^{3+}/\text{Cr}^{3+}$ ions on the crystal structure of BFO since it is a highly sensitive technique to get an idea about the atomic displacements, structural phase transitions, lattice properties, and spin-phonon coupling, change in bond lengths and bond angles. The rhombohedral crystal structure of BFO samples with the $R3c$ space group has been confirmed by the Rietveld refinement analysis of the XRD data. As per the group theory, BFO with $R3c$ space group in the rhombohedral distorted perovskite structure should display thirteen active optical phonon modes as given by $\Gamma_{\text{opt}}(R3c) = 4A_1^{\text{IR,R}} + 9E^{\text{IR,R}} + 5A_2$, here both E and A_1 modes are IR and Raman active, whereas A_2 are IR and Raman inactive [38]. In addition, these E and A_1 phonon modes are transverse optical (TO) vibrational modes. Using the deconvolution of the measured Raman spectra into various Lorentzian constituents for all the samples, the frequency of present Raman active modes has been obtained. The Raman spectra of BFO, BLFO, BLFCO2, BLFCO4, and BLFCO6 samples were recorded at room temperature and displayed in Fig. 3 along with the deconvoluted plots. It is evident that the Raman spectra of La/Cr co-doped BFO samples display quite different features as compared to the parent BFO sample.

In this study, 12 specific Raman active modes E-1, E-2, A_1 -1, A_1 -2, E-3, E-4, E-5, E-6, A_1 -4, E-7, E-8 and E-9 of BFO at frequencies 77, 108, 140, 172, 219, 270, 310, 350, 408, 468, 553 and 606 cm^{-1} , respectively are noted. The positions of all the Raman active modes are consistent with the previous reports [11, 29, 39]. Moreover, the number of Raman active modes present in the doped samples remains the same, demonstrating no structural phase transition, as is also established through the Rietveld refinement of XRD data. Raman active modes, E-1, E-2, A_1 -1 and A_1 -2 present at 77, 108, 140 and 172 cm^{-1} , respectively control the ferroelectric phase and dielectric constant of BFO that are governed by the Bi–O covalent bonds. A slight change in the position of Raman active modes, as mentioned in Table 2 with the doping signifies structural distortion of the BFO system. The Bi atoms contribute at the lower wavenumbers up to 167 cm^{-1} and above 262 cm^{-1} , oxygen motion

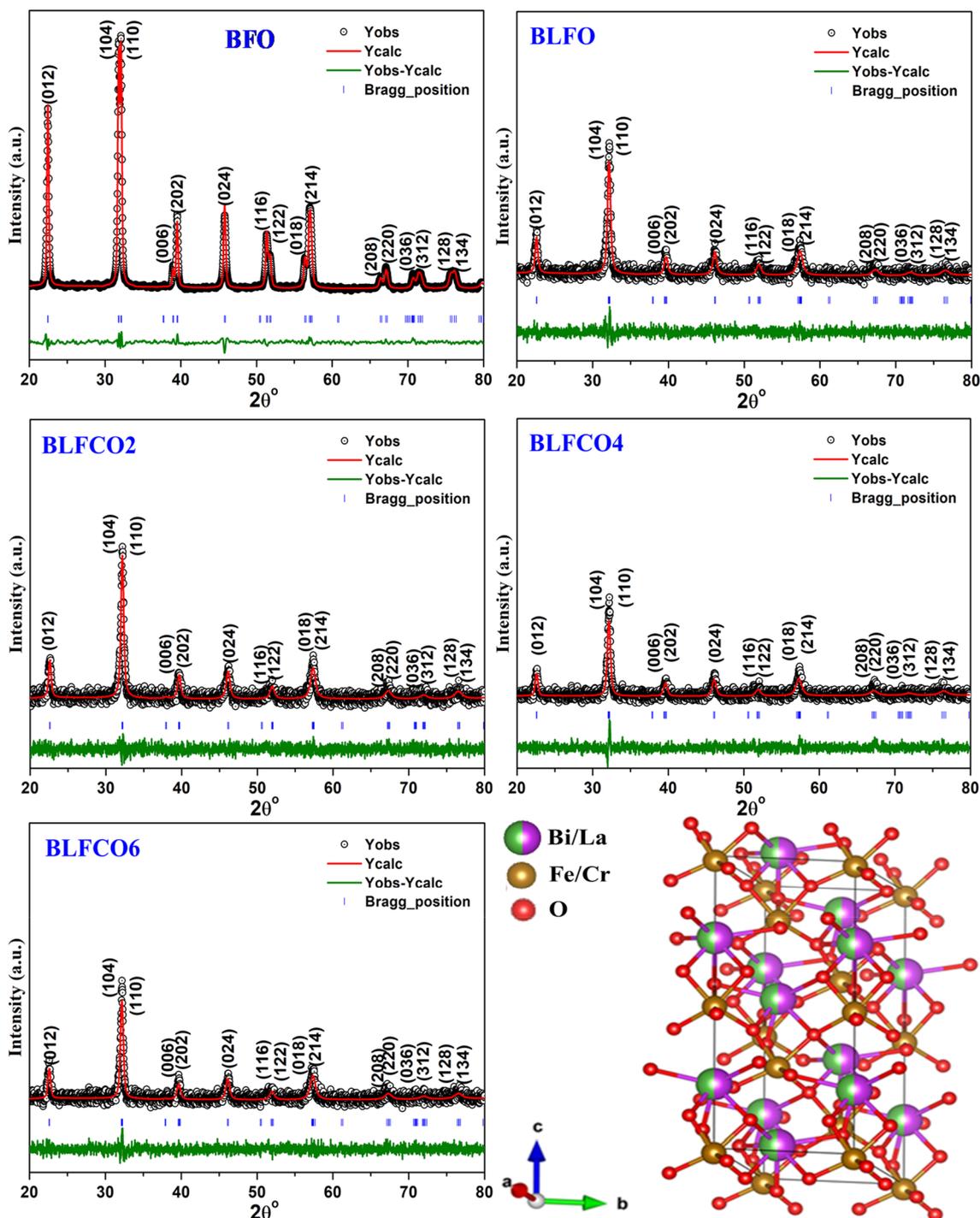


Fig. 2 Rietveld refined XRD patterns of BFO, BLFO, BLFCO2, BLFCO4, and BLFCO6 samples and schematic representation of crystal structure of the BLFCO2

dominates. Generally, the Fe atoms contribute to the frequency range of 152 to 262 cm^{-1} with a possible contribution at higher frequencies [39]. The shifting in modes position is managed through the local factors that incorporate the force constant related to the reduced mass (μ) as well

as bond strength, since the mode frequencies are proportional to $(k/\mu)^{1/2}$ (here k stands for the force constant). As the atomic weight of Fe (55.845 g/mol) is almost 7.40% more than that of Cr (51.996 g/mol), and similarly the atomic weight of Bi (208.98 g/mol) is about 50.443% higher than

Table 1 Rietveld refined structural parameters of BFO, BLFO, BLFCO2, BLFCO4, and BLFCO6 samples using rhombohedral crystal structure with space group R3c

Sample	Lattice parameters and unit cell volume	Atoms	Positions (x, y, z)			R-factors		Bond length Fe–O (Å)	Bond angle Fe–O–Fe (°)	χ^2
BFO	$a=5.5757(2) \text{ \AA}$	Bi	6a	0.0	0.0	0.0034	$R_{wp} = 3.30$	2.0	142.0	0.24
	$c=13.8595(1) \text{ \AA}$	Fe	6a	0.0	0.0	0.2258	$R_F = 2.12$			
	$V=373.1540 (\text{ \AA})^3$	O	18b	0.4905	0.0308	0.9493	$R_p = 2.57$			
BLFO	$a=5.5633(1) \text{ \AA}$	Bi/La	6a	0.0	0.0	0.2181	$R_{wp} = 12.2$	2.05	155.94	1.29
	$c=13.6495(3) \text{ \AA}$	Fe	6a	0.0	0.0	0.4832	$R_F = 7.97$			
	$V=365.8580 (\text{ \AA})^3$	O	18b	0.3696	0.0522	0.9229	$R_p = 9.57$			
BLFCO2	$a=5.5759(4) \text{ \AA}$	Bi/La	6a	0.0	0.0	0.2279	$R_{wp} = 11.7$	2.25	153.0	1.24
	$c=13.5744(2) \text{ \AA}$	Fe/Cr	6a	0.0	0.0	0.4815	$R_F = 7.55$			
	$V=365.5020 (\text{ \AA})^3$	O	18b	0.3239	0.0533	0.9229	$R_p = 9.34$			
BLFCO4	$a=5.5625(4) \text{ \AA}$	Bi/La	6a	0.0	0.0	0.2316	$R_{wp} = 14.9$	2.17	153.82	1.27
	$c=13.6379(2) \text{ \AA}$	Fe/Cr	6a	0.0	0.0	0.4802	$R_F = 11.0$			
	$V=365.4390 (\text{ \AA})^3$	O	18b	0.3481	0.0529	0.9236	$R_p = 12.0$			
BLFCO6	$a=5.5667(3) \text{ \AA}$	Bi/La	6a	0.0	0.0	0.2239	$R_{wp} = 13.6$	2.16	150.8	1.31
	$c=13.6210(1) \text{ \AA}$	Fe/Cr	6a	0.0	0.0	0.4795	$R_F = 9.95$			
	$V=365.5430 (\text{ \AA})^3$	O	18b	0.4056	0.0555	0.9154	$R_p = 10.8$			

that of La (138.91 g/mol), hence the co-substitution of La^{3+} and Cr^{3+} ions at Bi^{3+} and Fe^{3+} sites may be responsible for the shift in the position of Raman active modes [40].

As the atomic weights of La and Cr are lower than the Bi and Fe, respectively, and the mode frequency is inversely proportional to the reduced mass that may be shifted all the modes towards the higher wavenumber in the doped samples. Another possibility of mode shifting is the creation of oxygen vacancies, lattice distortion and change in the bond lengths and bond angles associated with the dopants concentrations [8, 29].

3.1.3 FTIR analysis

To determine the fundamental vibrations and related rotational-vibrational bands in the samples, the FTIR spectra are recorded and presented in Fig. 4 for BFO, BLFO, BLFCO2, BLFCO4 and BLFCO6 samples in the wavenumber range of 400–4000 cm^{-1} . These spectra show various characteristic vibrational absorption bands in all the prepared samples. The spectra of pristine BFO sample establish that the characteristic peaks are present at 445, 559, 1473, 1636, 2930, and 3413 cm^{-1} while for BLFCO6 sample, the peaks are observed at 477, 570, 849, 1462, 1688, 2930 and 3470 cm^{-1} . In the range of 3250 to 3600 cm^{-1} , the wide band is described to O–H stretching. However, the absorption peaks around 1473 and 2930 cm^{-1} are allocated to C–H vibrations, and the other band present at 1636 cm^{-1} is assigned to the C=O vibrations. An additional band observed at ~ 849 may be attributed to NO_3^- ions trapped in BFO nanoparticles [33, 37]. The broad absorption bands around 445 and 559

cm^{-1} are separately attributed to the bending and stretching vibrations of the Fe–O and Bi–O bonds that signify characteristics of the octahedral FeO_6 and BiO_6 groups respectively and affirm the formation of perovskite BiFeO_3 [40]. It is quite clear from these spectra that the absorption of the metal oxide band with La/Cr content increases.

Also, a slight shift of the absorption bands has been noticed towards higher wavenumber as Cr content increases that might be because of the creation of oxygen vacancies in the sample and disturbance occurring in the bonds. These outcomes are reliable according to previously reported results [8, 41].

3.2 Magnetic properties

The influence of La/Cr substitution on the magnetic behavior of BFO is studied using field-dependent magnetic measurements at 300 K with a maximum field of 18.3 kOe for all the samples. The observed magnetic hysteresis (M – H) loops of BFO, BLFO, BLFCO2, BLFCO4, and BLFCO6 samples are presented in Fig. 5a. All the loops clearly exhibit saturation of magnetization at higher values of the magnetic field except for pristine BFO. It signifies the ferromagnetic nature of the samples, excluding BFO. Since BiFeO_3 is a G-type antiferromagnetic material. In BiFeO_3 , every Fe^{3+} spin is enclosed by six canted antiparallel spins of the adjacent Fe atoms that contribute to the net magnetization. The magnetic moments of Fe^{3+} ions in BFO are coupled antiferromagnetically among the neighboring planes, while ferromagnetically in the pseudo-cubic (111) planes and six O^{2-} ions surround the Fe^{3+} ion and O^{2-} ion is the common top of two

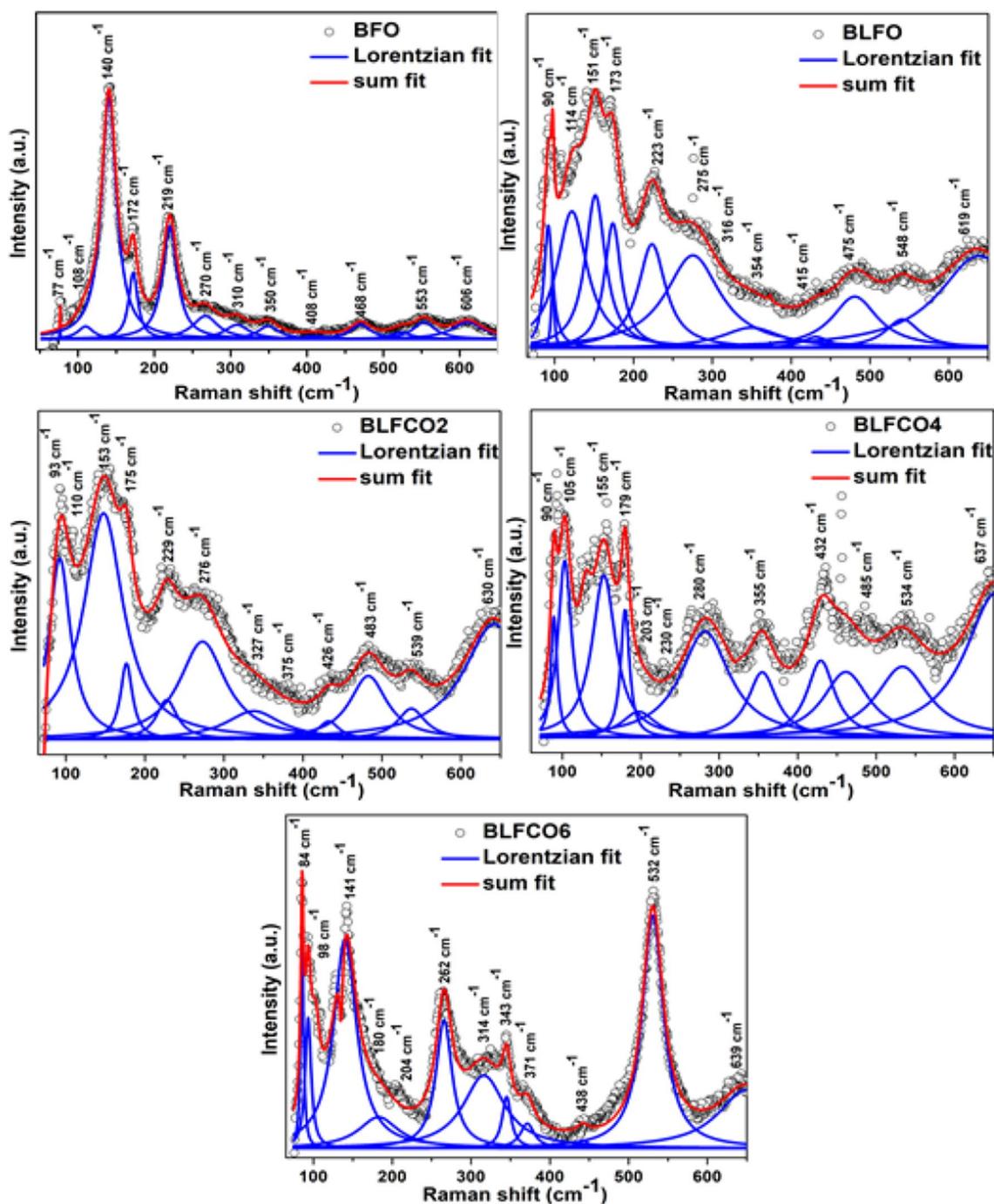


Fig. 3 Room temperature Raman and deconvoluted spectra of BFO, BLFO, BLFCO2, BLFCO4, and BLFCO6 samples

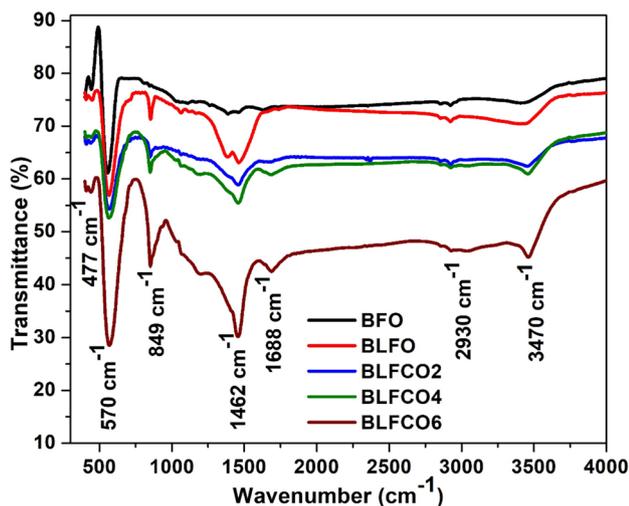
adjacent FeO_6 octahedra. Further, the superposition of space modulated spin structure with G-type antiferromagnetic spin ordering obstruct to obtain the magnetoelectric effect and net magnetization.

The improved magnetic moment is observed for all La/Cr co-doped BFO samples as compared to pristine BFO. The enlarged view of $M-H$ loops displayed in one of the insets of Fig. 5a reveals a nonzero coercivity (H_c) and remanent

magnetization (M_r) in all the samples. The different magnetic parameters like saturation magnetization (M_s), H_c , M_r , and magnetic moment per formula unit (μ_f) were assessed and summarized in Table 3 [8]. It is quite clear that the BLFO has the highest magnetization as compared to all other samples. The value of M_s of BLFO sample is observed to be 4.07 emu/g that is almost 58 times higher than pristine BFO (0.07 emu/g). This may be owing to the increase in

Table 2 The observed Raman active modes in BFO, BLFO, BLFCO2, BLFCO4, and BLFCO6 samples

Raman mode	Raman shift (cm ⁻¹)				
	BFO	BLFO	BLFCO2	BLFCO4	BLFCO6
E-1	77	90	93	90	84
E-2	108	114	110	105	98
A ₁ -1	140	151	153	155	141
A ₁ -2	172	173	175	179	180
A ₁ -3	–	–	–	203	204
E-3	219	223	229	230	262
E-4	270	275	276	280	314
E-5	310	316	327	–	343
E-6	350	354	375	355	371
A ₁ -4	408	415	426	432	438
E-7	468	475	483	485	–
E-8	553	548	539	534	532
E-9	606	619	630	637	639

**Fig. 4** FTIR spectra of BFO, BLFO, BLFCO2, BLFCO4, and BLFCO6 samples

the magnetization for La³⁺ doped BFO, associated with the suppression of the spiral spin structure and oxygen vacancies created due to the fluctuation in the statistical distribution of Fe³⁺/Fe²⁺ ions [38]. The doping of smaller radii ions, La³⁺ (1.16 Å) in our case at Bi³⁺ (1.17 Å) site, reduces the average A-site ionic radius of BFO that results in the reduction of the tolerance factor as reflected in the XRD patterns. This gives rise to the octahedral tilt and variation in the Fe–O bond lengths and Fe–O–Fe bond angles. The change in the bond angles and bond lengths influences the superexchange interaction between two antiferromagnetically aligned Fe³⁺ ions with a finite probability of canted structure that, in turn, suppresses of the space modulated spin structure [42].

The occurrence of the ferromagnetic nature in all the La/Cr co-doped BFO samples is based on the ferromagnetic Fe²⁺-O²⁻-Fe³⁺ double exchange interaction via the oxygen ion between the Fe²⁺ (3d⁶, *S* = 2) and Fe³⁺ (3d⁵, *S* = 5/2) ions. In addition, the improvement in the saturation magnetization might be related to the demolition of the space-modulated spin structure in BFO with La³⁺ and Cr³⁺ doping. As changes observed in the bond angle (Fe–O–Fe) and bond length (Fe–O) in Rietveld refinement of XRD data may be the cause of the distortion induced by the La³⁺ doping. The enhanced magnetization for all the La/Cr co-doped samples might be a result of the structural distortion produced by the dopants ions in BFO. The co-doping brings about the contraction of the unit cell that outcomes in a change in O–Fe–O bond angle as observed from the Rietveld refinement of the XRD data shown in Table 1, which may release the latent magnetization locked in the cycloidal spiral structure, resulting in an enhancement in magnetization. These may be the possible cause of the higher values of the magnetization in La/Cr co-doped BFO as compared to the pristine BFO. A saturated ferromagnetic hysteresis loop has been observed at a maximum field of 18.3 kOe with a magnetization of 4.07 emu/g and coercivity 150 Oe for the BLFO sample. The value of observed magnetization in the present study is more than that of various recently published reports on La-doped BFO multiferroic [11, 43].

Since Arrott–Belov–Kouvel (ABK) plots help to identify the magnetic state and order of the transition of the material, we have examined the nature of the *M*² versus *H/M* plots according to Banerjee criterion [29]. If the slope of the ABK plot is positive then the magnetic transition is of second order while for negative the transition is first order. We have plotted the graph presented in Fig. 5b between *M*² and *H/M* for all the samples using the *M*–*H* data. As the curvature and slope of the high field linear regions of the *M*² versus *H/M* reveal the magnetic state and transition of the samples. The concave nature without any spontaneous magnetization at *H* = 0 of the ABK plot signifies the antiferromagnetic nature, while plot for the ferromagnetic case exhibits a convex nature with spontaneous magnetization with a positive intercept of *M*² axis at *H* = 0. In the present case, the concave nature without spontaneous magnetization at *H* = 0 specifies the antiferromagnetic nature of the BFO sample. Other than BFO, the rest of the samples reveal positive intercept that suggests ferromagnetic nature, while positive slope of all the samples signifies second order magnetic transition according to the Banerjee criterion [29, 44].

To realize the ferromagnetic contribution to the *M*–*H* hysteresis loops of the samples, we have fitted the experimental data according to the Eq. (4) as given below [45], and linear contributions from antiferromagnetic/paramagnetic parts are deducted.

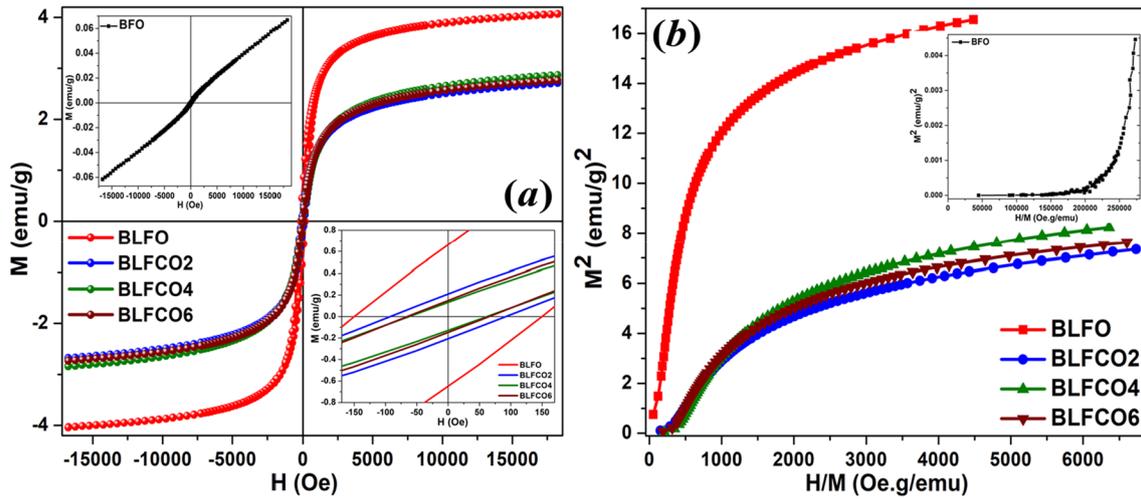


Fig. 5 a Room-temperature $M-H$ loops, and b ABK plots of BFO, BLFO, BLFCO2, BLFCO4, and BLFCO6 samples

$$M(H) = \left[\frac{2M_s}{\pi} \tan^{-1} \left\{ \left(\frac{H \pm H_c}{H_c} \right) \tan \left(\frac{\pi M_r}{2M_s} \right) \right\} \right] + \chi H \tag{4}$$

Here H , M , and χ stand for the applied magnetic field, magnetization, and magnetic susceptibility of antiferromagnetic/paramagnetic part, respectively. Apart from this, the first and second terms on the right-hand side of Eq. (4) represent the ferromagnetic as well as antiferromagnetic/paramagnetic contributions, respectively. Figures 6a, b show the fitted $M-H$ loops with experimental data and simulated antiferromagnetic and ferromagnetic contributions of the BLFO sample. In the case of the other samples, a similar procedure

has been adopted to analyze the $M-H$ data. In this manner, the significant magnetic parameters from the theoretical fitting of the experimental data were extracted and tabulated in Table 3.

3.3 Optical properties

It is a well-known fact that the optical behavior of materials is related to the microstructure and considered as an essential feature in determining the band gap. The optical properties of the samples were examined by the UV–visible diffuse reflectance spectroscopy (DRS) in the wavelength range of 350–700 nm that depicts the electronic structure of the materials. Further,

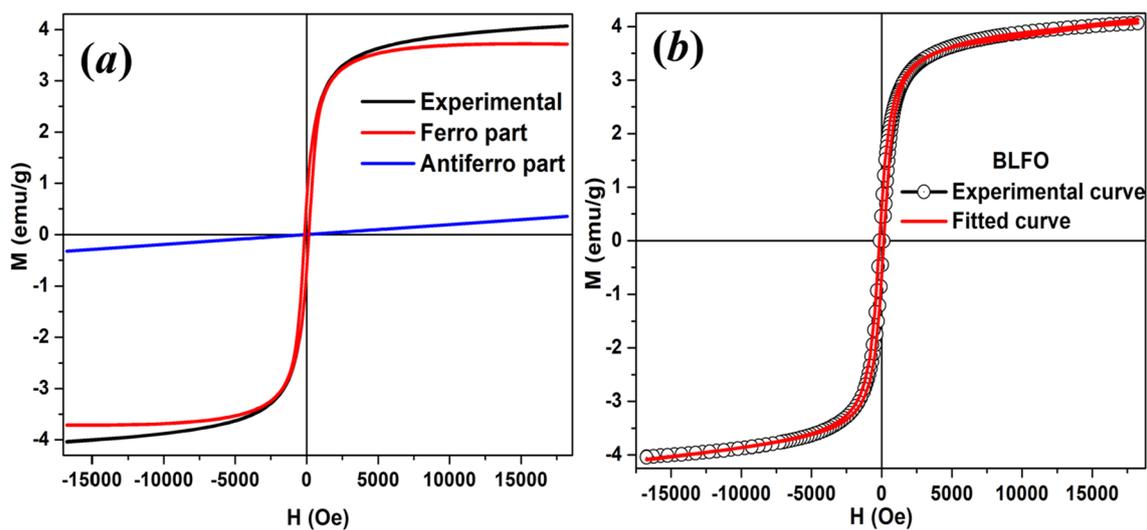


Fig. 6 $M-H$ loops of BLFO sample observed at room temperature, a experimental curve, contribution of ferro and antiferromagnetic parts, and b experimental data fitted with Eq. (4)

Table 3 The magnetic parameters: remanent magnetization (M_r), saturation magnetization (M_s), coercive field (H_c), magnetic moment per formula unit (μ_f), and magnetic susceptibility (χ) of BFO, BLFO, BLFCO2, BLFCO4, and BLFCO6 samples

Sample	Experimental				Theoretical			
	M_r (emu/g)	M_s (emu/g)	H_c (Oe)	$\mu_f \times 10^{-2}$ (μ_B)	M_r (emu/g)	M_s (emu/g)	H_c (Oe)	χ (emu/g-Oe) $\times 10^{-6}$
BFO	8.3×10^{-4}	0.07	113	0.39	6.5×10^{-4}	0.07	108	3.3
BLFO	0.66	4.07	150	20.24	0.62	4.13	153	25.6
BLFCO2	0.21	2.71	92	13.48	0.19	2.79	97	32.1
BLFCO4	0.13	2.87	62	14.26	0.14	2.95	79	33.2
BLFCO6	0.15	2.76	65	13.73	0.14	2.84	70	30.6

these UV–visible DRS spectra were transformed from the diffuse spectra to the corresponding Kubelka–Munk function [46], $F(R) = (1-R)^2/2R$, (here R stands for the diffuse reflectance) to obtain the equivalent energy band gap. Figure 7a shows the absorption spectra of all the samples that reveal a strong absorption in the broad wavelengths of the visible region from 350 to 550 nm. It is known that the materials exhibit strong absorption in the visible region are potential competitors to be used in optical applications, e.g., solar cells, photocatalysis, and so on. The uncertain state of the spectrum demonstrates that the observable light absorption happens by virtue of movement of an electron from the valence to the conduction band of BFO. Figure 7a also exhibits a redshift in the absorption edge as La/Cr content increases in BFO that may be attributed to the diffusion of the interface [37]. The absorption coefficient (α) is the highest significant optical parameter close to the band edge that follows the Tauc's relation [33] given by;

$$\alpha h\nu = k(h\nu - E_g)^n \quad (5)$$

where k is a constant, $h\nu$ is the energy of the incident photon, E_g is the band gap, and n describes the transition process. The values of n for direct and indirect bandgap transition are $1/2$ and 2, respectively.

The bandgap (E_g) of all the synthesized samples is estimated using Eq. (5). It is an established fact that BFO is a direct bandgap material, consequently, $n = 1/2$ has been taken for the evaluation of E_g . The equivalent values of E_g for all the samples have been evaluated from $(F(R)h\nu)^2$ versus $h\nu$ plots by the extrapolation of the linear region to $(F(R)h\nu)^2 \rightarrow 0$ as demonstrated in Fig. 7b. The obtained value of is 2.29 eV for pristine BFO that decreases as La/Cr concentration increases, and the values are summarized in Table 4. These results are consistent with the XRD data analysis, where crystallite size increases for the co-doped samples. Further, based on the quantum confinement and substitutional impacts, one can say that an increase in the crystallite size leads to the reduction of the energy bandgap. The reduction of the bandgap may be related to the existence of defect-induced energy levels close to the conduction band and an increase in the crystallite size of the BFO with the increase

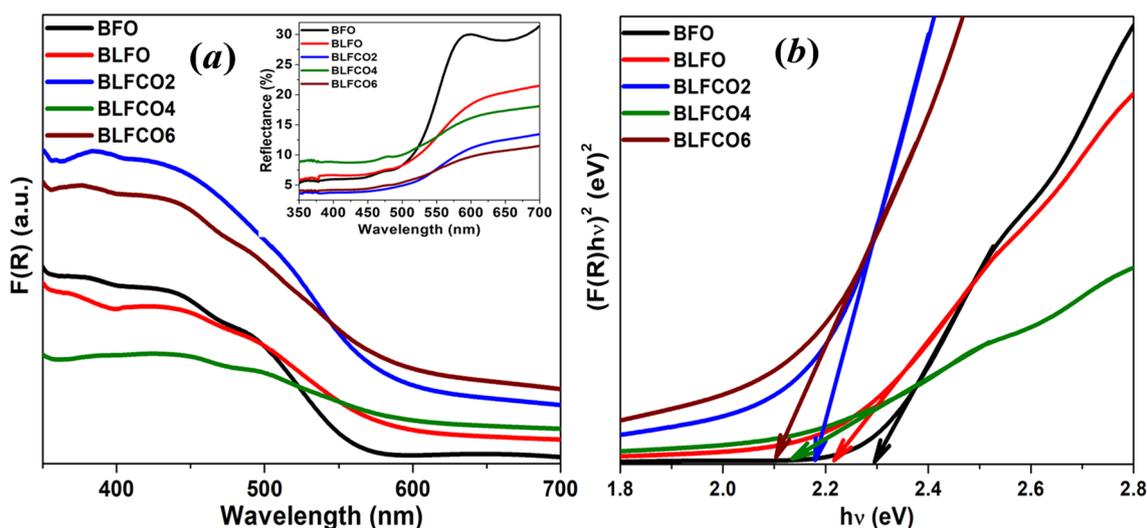


Fig. 7 a UV–visible DRS spectra, and b Tauc's plots of BFO, BLFO, BLFCO2, BLFCO4, and BLFCO6 samples. Inset shows a variation of reflectance (R) as a function of wavelength

in co-doping of La/Cr. Moreover, change in the band gap may be due to various reasons such as structural distortion produced, change in the particle size, and oxygen vacancies. The lattice distortion produced due to the co-substitution of La/Cr in BFO matrix because of the difference in atomic radii leads to change in the band gap. In addition, the fluctuated valence state of Fe i.e. $\text{Fe}^{2+}/\text{Fe}^{3+}$ leads to the creation of the oxygen vacancies. One more factor that may affect the band gap is the oxygen vacancies and it varies inversely to the oxygen vacancies. These outcomes are in great concurrence with the already reported values of the bandgap of BFO nanoparticles [33, 40].

Moreover, the reduction in band gap can also be ascribed to the appearance of certain imperfections related to the La and Cr doping that produce localized states in the band-gap region. Since Urbach energy (E_u) is an important optical factor to have a thought of the localized states in the bandgap because of feasible vacancies or defects impact on doping. As indicated by Urbach law, the absorption coefficient (α) near the band edges is an exponential character, and corresponding energy is referred as Urbach energy, i.e., $\alpha = \alpha_0 \exp(h\nu/E_u)$ [47]. In this way, E_u has been evaluated with the help of the absorption peak of the graph between $\ln\alpha$ and $h\nu$ (Fig. 8). In the case of all the samples, the value of E_u has been determined using the reciprocal of the slope of the graph. The occurrence of the Urbach energy tail is an indication of the widening of donor levels into defects band that converge with the conduction band. The higher estimation of E_u is associated with a higher density of localized states. In this case, an increase in the Urbach energy has been observed with the doping of La/Cr ions, and the calculated value of E_u near the edge is 144.73 meV for pristine BFO sample and 1298.84 meV for BLFCO6 sample. The increase in the value of E_u values suggests that the La/

Cr doping introduces defects and a greater number of localized states in BiFeO_3 . Further, Urbach energy can be written as $E_u = k_B T/S(T)$, where $S(T)$ is the steepness parameter [47]. The evaluated values of E_u and $S(T)$ are summarized in Table 4 for all the samples.

3.4 Ferroelectric properties

To confirm the multiferroic nature and to explore the influence of La/Cr co-doping on BFO, the room temperature polarization versus electric field (P – E) measurements were performed. The P – E loops observed at different applied electric fields for BFO, BLFO, BLFCO2, BLFCO4, and BLFCO6 samples at a frequency of 50 Hz are presented in Fig. 9. The observed P – E loops of all the samples indicate the presence of ferroelectricity at room temperature. Since the composition of all the samples is different, every sample exhibit different hysteresis nature because of the different breakdown fields.

The rise of the applied electric field reveals enhancement in the remanent polarization (P_r), maximum polarization (P_m), and coercivity (E_c) for BFO, BLFO, BLFCO2,

Table 4 The crystallite size (δ), tolerance factor (τ), bandgap (E_g), Urbach energy (E_u), and steepness parameter $S(T)$ for BFO, BLFO, BLFCO2, BLFCO4, and BLFCO6 samples

Sample	δ (nm)	τ	E_g (eV)	E_u (meV)	$S(T) \times 10^{-3}$
BFO	15	0.8886	2.29	144.73	178.68
BLFO	17	0.8869	2.21	407.08	63.53
BLFCO2	19	0.8872	2.18	552.30	46.82
BLFCO4	22	0.8874	2.13	836.62	30.91
BLFCO6	20	0.8877	2.10	1298.84	19.91

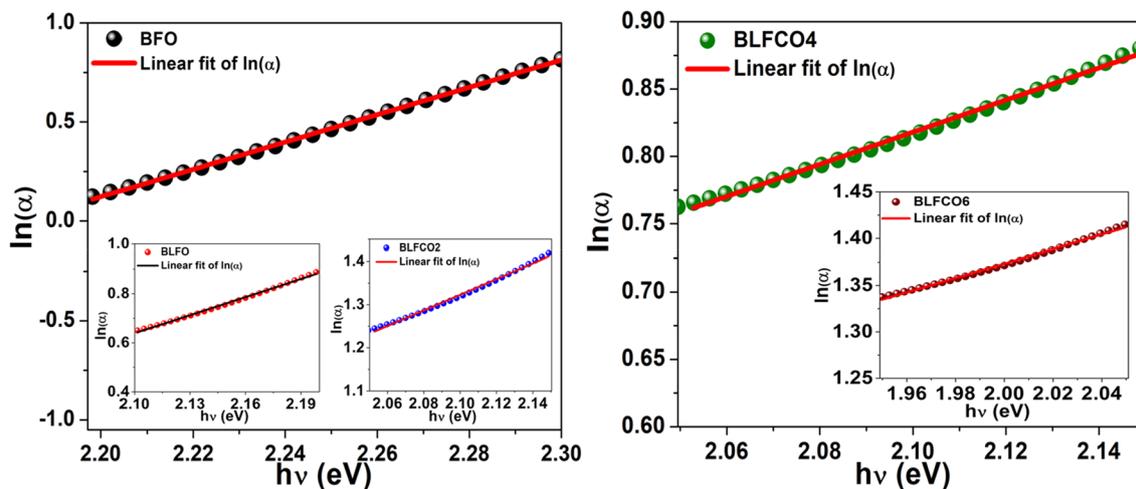


Fig. 8 $\ln\alpha$ versus $h\nu$ plots to determine the Urbach energy of BFO, BLFO, BLFCO2, BLFCO4, and BLFCO6 samples

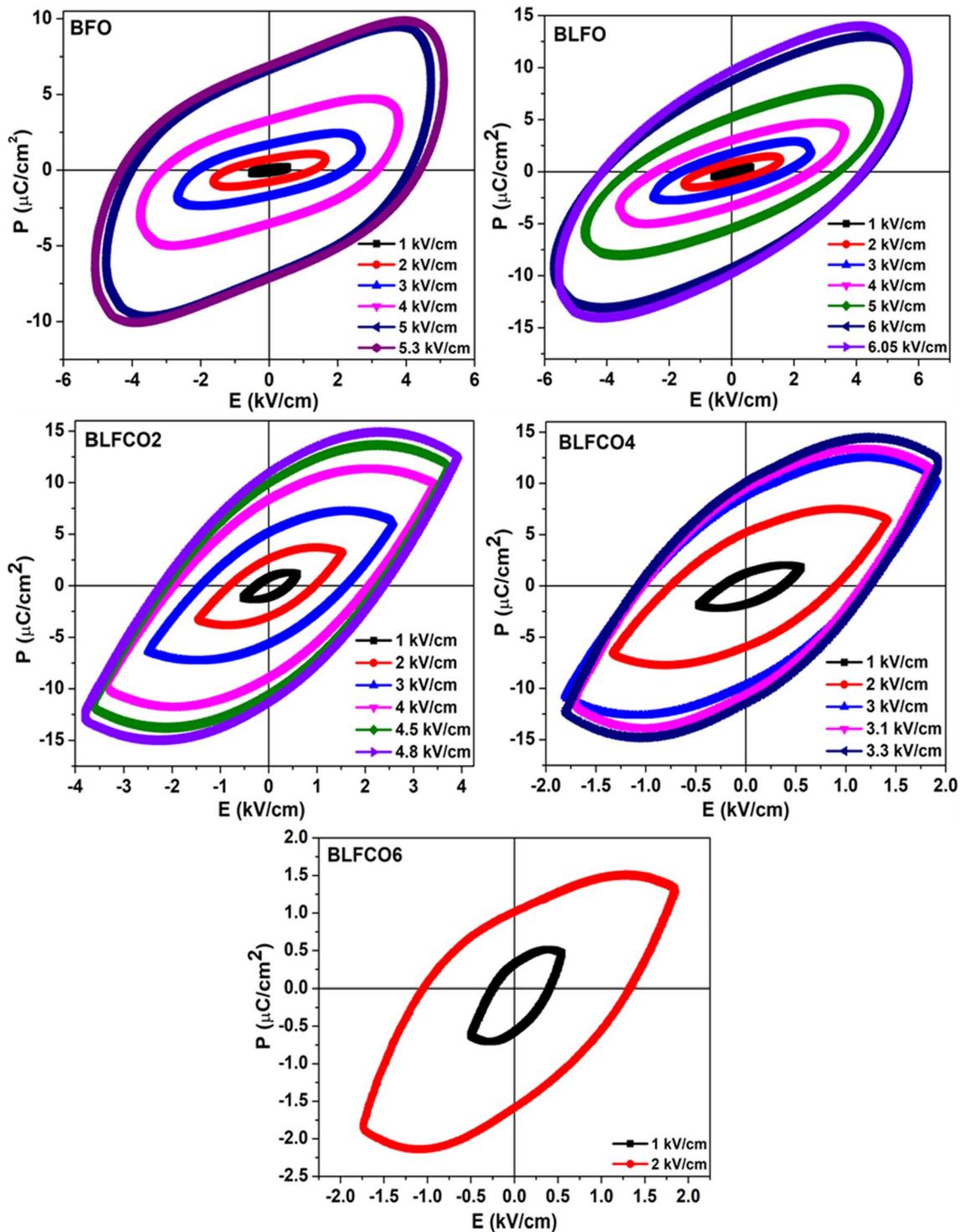


Fig. 9 P - E loops of BFO, BLFO, BLFCO2, BLFCO4, and BLFCO6 samples at different applied fields

BLFCO4, and BLFCO6 samples. This may be because of the larger applied electric field that allows, the higher level of driving force responsible for the reversal of ferroelectric domains [38, 48]. All the P - E loops exhibit ferroelectric behavior of the BFO, BLFO, BLFCO2, BLFCO4, and

BLFCO6 samples. These outcomes reveal that the doping of La and Cr at Bi and Fe sites, respectively, in BiFeO_3 brings about improved ferroelectric properties. It is quite clear from Fig. 9 that unsaturated ferroelectric loops are observed. Additionally, an increase in the remanent polarization and

maximum polarization for the La/Cr co-doped BFO has been noticed. The values of remanent polarization, maximum polarization, and coercive field at different applied fields are summarized in Table 5 for all the samples. The values of $2P_r$, $2P_m$, and $2E_c$ are found to be $14.04 \mu\text{C}/\text{cm}^2$, $20.0 \mu\text{C}/\text{cm}^2$ and $8.70 \text{ kV}/\text{cm}$ respectively at an applied field of $5.3 \text{ kV}/\text{cm}$ for the BFO sample. It can be noticed from Table 5 that the values of P_r , P_m , and E_c are higher for BLFO, BLFCO2, BLFCO4, and BLFCO6 samples in comparison with pristine BFO. This enhancement in ferroelectricity for all the co-doped BFO samples can be ascribed to the lower oxygen vacancies on account of La^{3+} and Cr^{3+} co-doping since the oxygen vacancies play a significant role in the pinning of polarization switching domains [30]. The saturated ferroelectric loops are not observed for BFO and La/Cr co-doped BFO samples because of the conductivity of BiFeO_3 that is attributed to the mixed states of Fe ions (Fe^{2+} to Fe^{3+}), results in higher leakage current due to the oxygen vacancies for charge compensation [49, 50]. The observed results demonstrate that a suitable percentage of doping can

be used to enhance the ferroelectric nature of the bismuth ferrite. These types of P-E loops have also been previously reported for the doped BiFeO_3 [50, 51] The increase of the ferroelectric polarization might be ascribed to the structural distortion occurs by the co-doping of La/Cr, as established from the XRD data analysis.

3.5 Dielectric properties

To understand the complex dielectric permittivity behavior of BFO, BLFO, and BLFCO4, temperature and frequency dependence of dielectric constant and loss tangent have been investigated. The complex permittivity can be stated as, $\epsilon^* = \epsilon' - j\epsilon''$, here $\epsilon' = C_p d/\epsilon_0 A$, stands for the real part of the permittivity (ϵ_0 is the permittivity of free space, C_p is the capacitance of the circular pellet, d and A are the thickness and cross-sectional area of the pellet respectively) whereas ϵ'' is the imaginary part of the permittivity. The dissipation factor or dielectric loss ($\tan\delta$) can be defined as, $\tan\delta = \epsilon''/\epsilon'$ [37]. A variation of the real part of the permittivity (ϵ') for BFO, BLFO and BLFCO4 samples as a function of temperature at selected frequencies (10 Hz, 100 Hz, 1 kHz, and 100 kHz) are presented in Figs. 10a, 11a and 12a and dielectric loss ($\tan\delta$) of all the samples are shown in Figs. 10b, 11b and 12b, respectively. The dielectric nature of the material depends on the synthesis process and its microstructure. These properties emerge as a result of an electric dipole moment, which builds up the charge exchange among trivalent and divalent cations within a structure. It can be seen from Fig. 10a that the dielectric constant, slowly increases with the rise in temperature up to 300 K and then a sharp increase occurs above 300 K. At 500 K, we have observed larger values of the real part of the dielectric constant as 8.88×10^7 , 2.30×10^6 , 6.40×10^4 and 266 at frequencies 10 Hz, 100 Hz, 1 kHz, and 100 kHz, respectively, for the pristine BFO sample. It is clear that the permittivity values for BLFO and BLFCO4 samples are lower than those of the BFO. It is apparent that the value of the real part of permittivity is decreased for the La/Cr co-doped BFO. Dielectric loss displays a similar trend for all the samples. Furthermore, a dielectric relaxation peak around 400 K has been observed for the BFO sample, and after that, a sharp increase in the dielectric constant is observed.

However, this peak appears at around 423 and 388 K in the case of BLFO and BLFCO4 samples, respectively. This dielectric relaxation peak is also observed in the dielectric loss versus temperature plots. A lower value (i.e. < 1) of the dielectric loss is found at 100 kHz, 500 K for all the samples. Accordingly, the dielectric loss and dielectric constants are strongly dependent on the percentage of La/Cr content. One can notice the presence of a sharp increase in the dielectric constant for the frequencies 10 Hz, 100 Hz, and 1 kHz while a lower value is observed for 100 kHz frequency in the

Table 5 The remanent polarization (P_r), maximum polarization (P_m), and coercive field (E_c) of BFO, BLFO, BLFCO2, BLFCO4, and BLFCO6 samples at different applied fields

Sample	Field (kV/cm)	$2P_r$ ($\mu\text{C}/\text{cm}^2$)	$2P_m$ ($\mu\text{C}/\text{cm}^2$)	$2E_c$ (kV/cm)
BFO	1.0	0.32	0.58	0.72
	2.0	1.49	2.17	2.52
	3.0	3.39	4.80	4.28
	4.0	6.85	9.75	6.29
	5.0	13.59	19.15	8.14
	5.3	14.04	20.00	8.70
	BLFO	1.0	0.61	1.00
2.0		1.81	3.00	1.93
3.0		3.55	5.66	3.32
4.0		6.34	9.70	4.98
5.0		10.70	15.92	6.74
6.0		17.91	26.02	8.35
6.05		18.65	27.96	8.40
BLFCO2	1.0	1.85	2.54	0.66
	2.0	5.62	6.54	1.78
	3.0	10.83	14.44	3.00
	4.0	16.24	23.13	4.05
	4.5	20.47	27.50	4.38
	4.8	22.32	29.95	4.61
BLFCO4	1.0	3.02	4.27	0.60
	2.0	11.20	15.17	1.66
	3.0	17.46	25.10	2.20
	3.1	20.20	27.23	2.26
	3.3	21.60	29.20	2.32
BLFCO6	1.0	0.90	1.22	0.65
	2.0	2.61	3.66	2.38

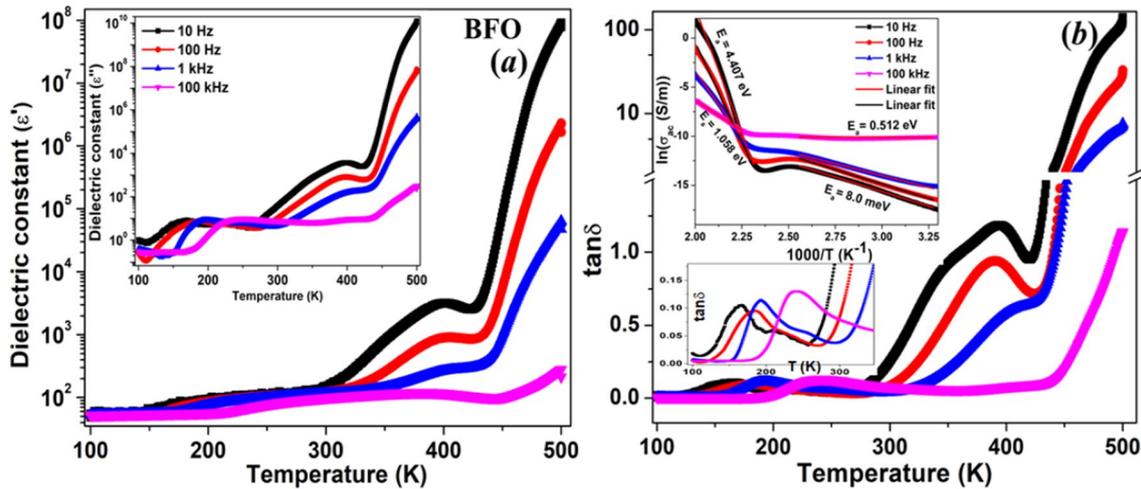


Fig. 10 Variation of the **a** real and imaginary (inset) parts of dielectric constants, and **b** dielectric loss as a function of temperatures for the BFO sample. The upper inset in **b** shows the plots of $\ln\sigma$ versus $10^3/K$, whereas lower inset is the zoom in view of the dielectric loss for the same

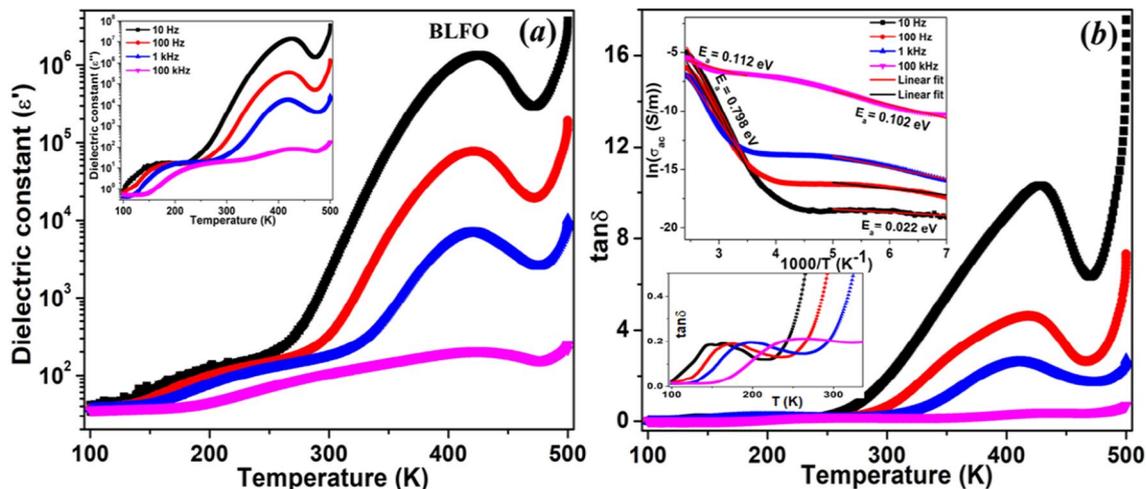


Fig. 11 Variation of the **a** real and imaginary (inset) parts of dielectric constants, and **b** dielectric loss as a function of temperatures for the BLFO sample. The upper inset in **b** shows the plots of $\ln\sigma$ versus

$10^3/K$, whereas lower inset is the zoom in view of the dielectric loss for the same

working temperature range. This lower value of the dielectric constant in this temperature range emerges because of grains impact.

The higher values of permittivity at lower frequencies and higher temperatures mainly emerge due to the Maxwell–Wagner polarization phenomenon [38]. With the rise in the temperature, the electrode effects and grain boundaries give rise to their permittivity values. Schottky barriers form interfaces between grains, grain boundaries, surface effects, and the presence of electrodes in the material. When a sample is sintered at a higher temperature, the outer surface of the pellet may get some oxygen stoichiometry, and resistance turns out to be higher than the inner part of the sample. These Schottky barriers have a very high capacitance as compared

to grains, subsequently, higher values of permittivity are noticed on the development of barriers [52]. These higher permittivity could be credited to the occurrence of a ferroelectric nature. It is clear from Fig. 12a that the permittivity decreases at higher frequencies while dispersion peak shifts towards the higher temperature for the BLFCO4 sample. A similar trend is also observed for dielectric loss, as evident from Fig. 12b. This behavior may be attributed to the thermally activated relaxation. We have also studied the data in the light of Arrhenius law, where $\ln\sigma$ is plotted as a function of $10^3/T$. The evaluated values of the activation energy (E_a) are found to be 4.41, 3.52, 2.33 and 1.06 eV for 10 Hz, 100 Hz, 1 kHz and 100 kHz respectively at higher temperature. While at lower temperatures, we have found these values

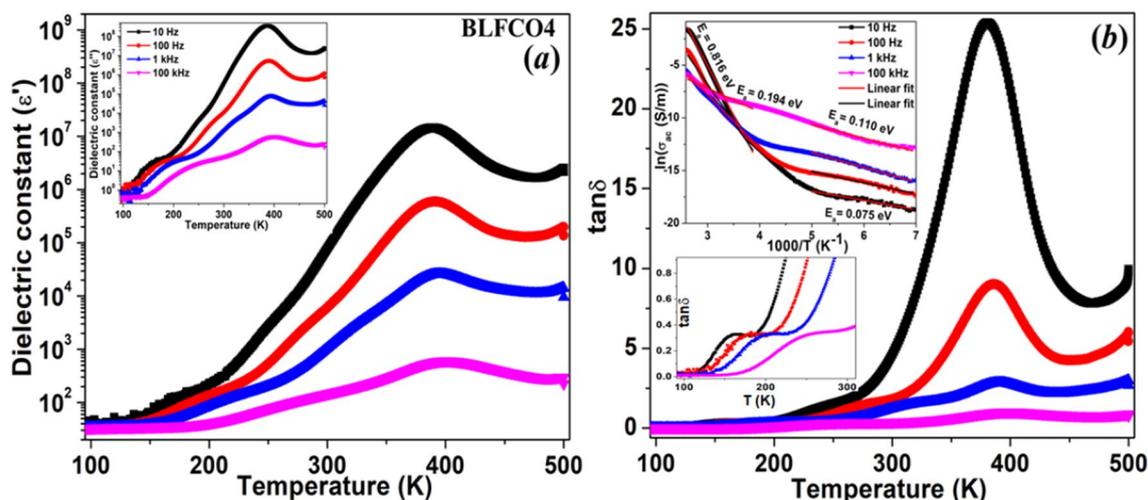


Fig. 12 Variation of the **a** real and imaginary (inset) parts of dielectric constants, and **b** dielectric loss as a function of temperatures for the BLFCO4 sample. The upper inset in **b** shows the plots of $\ln \sigma$ ver-

sus $10^3/K$, whereas lower inset is the zoom in view of the dielectric loss for the same

as 0.51, 0.51, 0.42 and 0.01 eV for 10 Hz, 100 Hz, 1 kHz and 100 kHz respectively for BFO sample (upper inset of Fig. 10b). This reveals that the increase in frequency reduces the activation energy of the system. Similar trend of the activation energy is also observed for the BLFO and BLFCO4 samples (upper insets of Figs. 11b, 12b respectively).

Besides, the lower value of the E_a in the lower temperature region can be attributed to the effect of electronic influence on conductivity. Then, the transportation of charge carriers may arise with the hopping of localized states in a disordered system [52, 53]. The temperature-dependent loss tangent of BFO, BLFO and BLFCO4 at few selected frequencies exhibits the well-defined dielectric peak at all the frequencies (lower insets of Figs. 10b, 11b and 12b). The presence of the peak in the temperature range of 100–300 K is the indication of conductive losses

because of relaxing dipoles in the samples. Moreover, dielectric peaks gradually shift towards the higher temperatures when the frequency increases from 10 Hz to 100 kHz or vice versa and confirms thermally activated relaxation mechanism in the system. The peaks of the dielectric loss observed in the low temperature region accompanied with a strong frequency dispersion are distinct features of relaxor ferroelectrics. In the relaxor ferroelectrics, the frequency dependence of the temperature corresponding to the maximum value of the dielectric loss (T_m) may be elucidated by the Vogel–Fulcher ($V-F$) relation [54]. To investigate the relaxation features of the La/Cr co-doped BFO nanostructures, we have fitted the experimental data displayed in Fig. 13 using $V-F$ relation given by:

$$f = f_0 \exp(-E_a/k_B(T_m - T_F)) \tag{6}$$

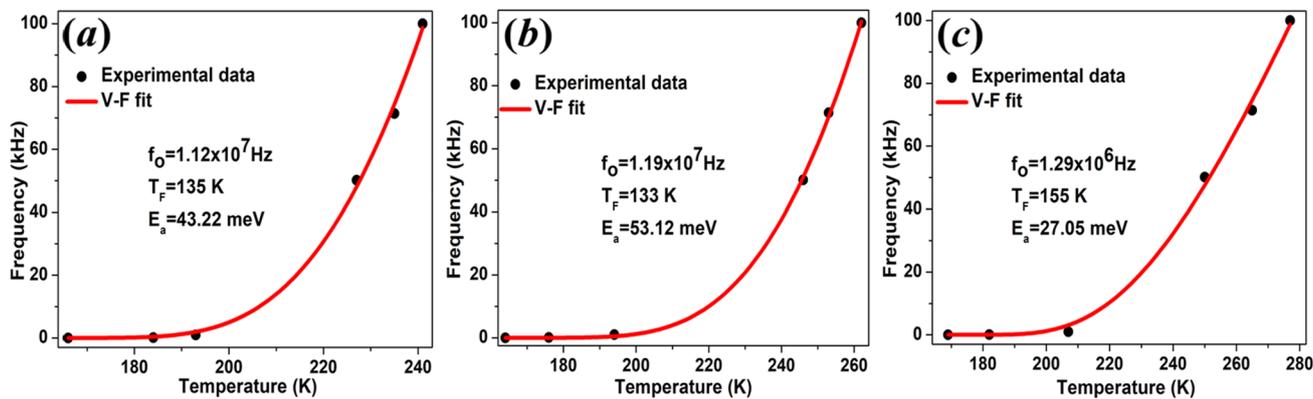


Fig. 13 The Vogel–Fulcher fitting of frequency as a function of T_m for **a** BFO, **b** BLFO, and **c** BLFCO4 samples

Here f and f_0 are the measured and Debye frequencies, respectively, T_F is the Vogel–Fulcher freezing temperature, k_B is the Boltzmann constant, and E_a is the activation energy describing the relaxation process. The obtained values of the parameters for the BFO sample are $f_0 = 1.12 \times 10^7$ Hz, $T_F = 135$ K, and $E_a = 43.22$ meV. While for the BLFO and BLFCO4 samples, the obtained values are $f_0 = 1.19 \times 10^7$ Hz, $T_F = 133$ K, and $E_a = 53.12$ meV and $f_0 = 1.29 \times 10^6$ Hz, $T_F = 155$ K and $E_a = 27.05$ meV respectively. Hence the temperature dependence of the relaxation time described through the Vogel–Fulcher model confirms that the dipolar response is a thermally activated process.

4 Conclusions

The single-phase BFO and La/Cr co-doped BFO samples have been successfully prepared via a low-temperature sol–gel process. The impact of La/Cr doping ions on the structural, multiferroic, optical, and dielectric properties of BFO was investigated in detail using various characterization techniques. Raman spectra and Rietveld refinement analysis of the XRD data support the single-phase nature of all the synthesized samples with the $R3c$ space group in the rhombohedral crystal system. Further, the formation of BiFeO_3 has been confirmed from the characteristic bands of FeO_6 and other vibrational bands in the FTIR spectra. The average crystallite/particle size was found to increase as La/Cr dopants increases while the band gap decreases. The enhanced dielectric properties are observed for the co-doped BFO samples. A very high value of the dielectric constant for pristine BFO is found to be of the order 10^8 at 10 Hz and at 500K temperature. The multiferroism in BFO and La/Cr co-doped BFO has been confirmed from the observed ferroelectric (P – E) and ferromagnetic (M – H) loops. The magnetization for the BLFO is found to be about 58 times of the pristine BFO. The enhanced magnetization might be because of changes observed in the bond lengths/angles, oxygen vacancies-related defects, $\text{Fe}^{2+}/\text{Fe}^{3+}$ exchange interactions, or the suppression of spin spiral structure because of nano-size particles. Furthermore, M – H data have been fitted theoretically to compare and extract several important magnetic parameters. Moreover, the highest polarization is found for the BLFCO4 sample at 1 kV/cm and 2 kV/cm. Hence, by the appropriate doping of La/Cr, the magnetic, ferroelectric, optical and dielectric properties can be tuned for potential applications.

Acknowledgements One of the authors, M. Nadeem is thankful to the Inter-University Accelerator Centre (IUAC), New Delhi, for financial support in the form of a project fellowship (UFR No. 61317). The authors would like to thank Dr. Vasant Sathe UGC-DAE CSR, Indore, for the Raman measurements.

References

1. S.W. Cheong, M. Mostovoy, Multiferroics: a magnetic twist for ferroelectricity. *Nat. Mater.* **6**, 13–20 (2007). <https://doi.org/10.1038/nmat1804>
2. M. Fiebig, T. Lottermoser, D. Meier, M. Trassin, The evolution of multiferroics. *Nat. Rev. Mater.* **1**, 1–14 (2016). <https://doi.org/10.1038/natrevmats.2016.46>
3. W. Eerenstein, N.D. Mathur, J.F. Scott, Multiferroic and magnetoelectric materials. *Nature.* **442**, 759–765 (2006). <https://doi.org/10.1038/nature05023>
4. H. Singh, K.L. Yadav, Dielectric, magnetic and magnetoelectric properties of La and Nb codoped bismuth ferrite. *J. Phys. Condens. Matter* **23**, 1–6 (2011). <https://doi.org/10.1088/0953-8984/23/38/385901>
5. R. Ramesh, N.A. Spaldin, Multiferroics: progress and prospects in thin films. *Nat. Mater.* **6**, 21–29 (2007). <https://doi.org/10.1038/nmat1805>
6. M. Kumar, K.L. Yadav, Study of room temperature magnetoelectric coupling in Ti substituted bismuth ferrite system. *J. Appl. Phys.* **100**, 23–26 (2006). <https://doi.org/10.1063/1.2349491>
7. A.K. Pradhan, K. Zhang, D. Hunter, J.B. Dadson, G.B. Lioiutts, P. Bhattacharya, R. Katiyar, J. Zhang, D.J. Sellmyer, U.N. Roy, Y. Cui, A. Burger, Magnetic and electrical properties of single-phase multiferroic BiFeO_3 . *J. Appl. Phys.* **97**, 093903 (2005). <https://doi.org/10.1063/1.1881775>
8. A. Anju, P. Agarwal, B. Aghamkar, Lal, Structural and multiferroic properties of barium substituted bismuth ferrite nanocrystallites prepared by sol–gel method. *J. Magn. Magn. Mater.* **426**, 800–805 (2017). <https://doi.org/10.1016/j.jmmm.2016.09.103>
9. D. Khomskii, *Classifying Multiferroics: Mechanisms and Effects*, Physics (College. Park. Md, 2009). 2, 20. <https://doi.org/10.1103/physics.2.20>
10. T. Kimura, T. Goto, H. Shintani, K. Ishizaka, T. Arima, Y. Tokura, Magnetic control of ferroelectric polarization. *Nature.* **426**, 55–58 (2003). <https://doi.org/10.1038/nature02018>
11. P. Suresh, S. Srinath, Effect of la substitution on structure and magnetic properties of sol-gel prepared BiFeO_3 . *J. Appl. Phys.* **113**, 17D920 (2013). <https://doi.org/10.1063/1.4801509>
12. S. Iakovlev, C.-H. Solterbeck, M. Kuhnke, M. Es-Souni, Multiferroic BiFeO_3 thin films processed via chemical solution deposition: Structural and electrical characterization. *J. Appl. Phys.* **97**, 094901 (2005). <https://doi.org/10.1063/1.1881776>
13. R. Das, T. Sarkar, K. Mandal, Multiferroic properties of Ba^{2+} and Gd^{3+} co-doped bismuth ferrite: magnetic, ferroelectric and impedance spectroscopic analysis. *J. Phys. D Appl. Phys.* **45**, 455002 (2012). <https://doi.org/10.1088/0022-3727/45/45/455002>
14. Y. Du, Z.X. Cheng, M. Shahbazi, E.W. Collings, S.X. Dou, X.L. Wang, Enhancement of ferromagnetic and dielectric properties in lanthanum doped BiFeO_3 by hydrothermal synthesis. *J. Alloys Compd.* **490**, 637–641 (2010). <https://doi.org/10.1016/j.jallcom.2009.10.124>
15. I.M. Sosnowska, Spatially modulated spin structure (SMSS) in BiFeO_3 -30 years later. *J. Phys. Condens. Matter* **28**, 421002 (2016). <https://doi.org/10.1088/0953-8984/28/42/421002>
16. S. Gupta, M. Tomar, V. Gupta, Magnetic hysteresis of cerium doped bismuth ferrite thin film. *J. Magn. Magn. Mater.* **378**, 333–339 (2015). <https://doi.org/10.1016/j.jmmm.2014.11.062>
17. R. Dhanalakshmi, M. Muneeswaran, P.R. Vanga, M. Ashok, N.V. Giridharan, Enhanced photocatalytic activity of hydrothermally grown BiFeO_3 nanostructures and role of catalyst recyclability in photocatalysis based on magnetic framework. *Appl. Phys. A Mater. Sci. Process.* **122**, 1–14 (2016). <https://doi.org/10.1007/s00339-015-9527-z>

18. M.M. Kumar, V.R. Palkar, K. Srinivas, S.V. Suryanarayana, Ferroelectricity in a pure BiFeO₃ ceramic. *Appl. Phys. Lett.* **76**, 2764–2766 (2000). <https://doi.org/10.1063/1.126468>
19. B. Yu, M. Li, J. Liu, D. Guo, L. Pei, X. Zhao, Effects of ion doping at different sites on electrical properties of multiferroic BiFeO₃ ceramics. *J. Phys. D Appl. Phys.* **41**, 065003 (2008). <https://doi.org/10.1088/0022-3727/41/6/065003>
20. X. Qi, J. Dho, R. Tomov, M.G. Blamire, J.L. MacManus-Driscoll, Greatly reduced leakage current and conduction mechanism in aliovalent-ion-doped BiFeO₃. *Appl. Phys. Lett.* **86**, 1–3 (2005). <https://doi.org/10.1063/1.1862336>
21. P.K. Jha, P.A. Jha, G. Srivastava, A.K. Jha, R.K. Kotnala, R.K. Dwivedi, Analytical comparison of magnetic and electrical properties using modified Landau theory in bismuth ferrite: effect of milling. *J. Magn. Magn. Mater.* **349**, 95–99 (2014). <https://doi.org/10.1016/j.jmmm.2013.08.048>
22. R.K. Mishra, D.K. Pradhan, R.N.P. Choudhary, A. Banerjee, Effect of yttrium on improvement of dielectric properties and magnetic switching behavior in BiFeO₃. *J. Phys. Condens. Matter* **20**, 045218 (2008). <https://doi.org/10.1088/0953-8984/20/04/045218>
23. A. Gautam, P. Uniyal, K.L. Yadav, V.S. Rangra, Dielectric and magnetic properties of Bi_{1-x}Y_xFeO₃ ceramics. *J. Phys. Chem. Solids* **73**, 188–192 (2012). <https://doi.org/10.1016/j.jpcs.2011.11.005>
24. Z.X. Cheng, A.H. Li, X.L. Wang, S.X. Dou, K. Ozawa, H. Kimura, S.J. Zhang, T.R. Shrout, Structure, ferroelectric properties, and magnetic properties of the La-doped bismuth ferrite. *J. Appl. Phys.* **103**, 07E507 (2008). <https://doi.org/10.1063/1.2839325>
25. Y. Kim, J. Won, C. Murugesan, J. Oak, H. Jin, W. Kim, M. Ho, T. Kwon, S. Su, Enhancement of electrical properties of (Gd, V) co-doped BiFeO₃ thin films prepared by chemical solution deposition. *Ceram. Int.* **39**, S195–S199 (2013). <https://doi.org/10.1016/j.ceramint.2012.10.061>
26. M.R. Islam, R.H. Galib, A. Sharif, M.H. Rizvi, M.A. Zubair, M.F. Islam, Correlation of charge defects and morphology with magnetic and electrical properties of Sr and Ta codoped BiFeO₃. *J. Alloys Compd.* (2016). <https://doi.org/10.1016/j.jallcom.2016.07.134>
27. P. Uniyal, K.L. Yadav, Pr doped bismuth ferrite ceramics with enhanced multiferroic properties. *J. Phys. Condens. Matter* **21**, 1–6 (2009). <https://doi.org/10.1088/0953-8984/21/40/405901>
28. Z. Yan, K.F. Wang, J.F. Qu, Y. Wang, Z.T. Song, S.L. Feng, Processing and properties of Yb-doped BiFeO₃ ceramics. *Appl. Phys. Lett.* **91**, 082906 (2007). <https://doi.org/10.1063/1.2775034>
29. H. Singh, K.L. Yadav, Enhanced magnetization with unusual low temperature magnetic ordering behaviour and spin reorientation in holmium-modified multiferroic BiFeO₃ perovskite ceramics. *J. Phys. D Appl. Phys.* **48**, 205001 (2015). <https://doi.org/10.1088/0022-3727/48/20/205001>
30. A. Mukherjee, S. Basu, P.K. Manna, S.M. Yusuf, M. Pal, Giant magnetodielectric and enhanced multiferroic properties of Sm doped bismuth ferrite nanoparticles. *J. Mater. Chem. C* **2**, 5885 (2014). <https://doi.org/10.1039/c4tc00591k>
31. N. Zhang, D. Chen, F. Niu, S. Wang, L. Qin, Y. Huang, Enhanced visible light photocatalytic activity of Gd-doped BiFeO₃ nanoparticles and mechanism insight. *Sci. Rep.* **6**, 1–11 (2016). <https://doi.org/10.1038/srep26467>
32. Z. Hu, D. Chen, S. Wang, N. Zhang, L. Qin, Y. Huang, Facile synthesis of Sm-doped BiFeO₃ nanoparticles for enhanced visible light photocatalytic performance. *Mater. Sci. Eng. B* **220**, 1–12 (2017). <https://doi.org/10.1016/j.mseb.2017.03.005>
33. M. Nadeem, W. Khan, S. Khan, M. Shueb, S. Husain, M. Mobin, Significant enhancement in photocatalytic performance of Ni doped BiFeO₃ nanoparticles. *Mater. Res. Express.* **5**, 065506 (2018). <https://doi.org/10.1088/2053-1591/aac70d>
34. K. Chakrabarti, K. Das, B. Sarkar, S. Ghosh, S.K. De, G. Sinha, J. Lahtinen, Enhanced magnetic and dielectric properties of Eu and Co co-doped BiFeO₃ nanoparticles. *Appl. Phys. Lett.* **101**, 042401 (2012). <https://doi.org/10.1063/1.4738992>
35. F. Lin, Q. Yu, L. Deng, Z. Zhang, X. He, A. Liu, W. Shi, Effect of La/Cr codoping on structural transformation, leakage, dielectric and magnetic properties of BiFeO₃ ceramics. *J. Mater. Sci.* **52**, 7118–7129 (2017). <https://doi.org/10.1007/s10853-017-0947-3>
36. N. Li, J. Wu, Y. Jiang, Z. Xie, L. Zheng, Z. Ye, Structure and multiferroic properties of Bi_(1-x)Dy_xFe_{0.90}Mg_{0.05}Ti_{0.05}O₃ solid solution. *J. Appl. Phys.* **113**, 054102 (2013). <https://doi.org/10.1063/1.4790326>
37. M. Abushad, W. Khan, S. Naseem, S. Husain, M. Nadeem, A. Ansari, Influence of Mn doping on microstructure, optical, dielectric and magnetic properties of BiFeO₃ nanoceramics synthesized via sol-gel method. *Ceram. Int.* **45**, 7437–7445 (2019). <https://doi.org/10.1016/j.ceramint.2019.01.035>
38. M. Nadeem, W. Khan, S. Khan, S. Husain, A. Ansari, Tailoring dielectric properties and multiferroic behavior of nanocrystalline BiFeO₃ via Ni doping. *J. Appl. Phys.* **124**, 164105 (2018). <https://doi.org/10.1063/1.5050946>
39. P. Hermet, M. Goffinet, J. Kreisel, P. Ghosez, Raman and infrared spectra of multiferroic bismuth ferrite from first principles. *Phys. Rev. B* **75**, 220102 (2007). <https://doi.org/10.1103/PhysRevB.75.220102>
40. P.C. Sati, M. Arora, S. Chauhan, S. Chhoker, M. Kumar, Structural, magnetic, and optical properties of Pr and Zr codoped BiFeO₃. *J. Appl. Phys.* **112**, 094102 (2012). <https://doi.org/10.1063/1.4761968>
41. J. Xu, H. Ke, D. Jia, W. Wang, Y. Zhou, Low-temperature synthesis of BiFeO₃ nanopowders via a sol-gel method. *J. Alloys Compd.* **472**, 473–477 (2009). <https://doi.org/10.1016/j.jallcom.2008.04.090>
42. T.D. Rao, T. Karthik, S. Asthana, Investigation of structural, magnetic and optical properties of rare earth substituted bismuth ferrite. *J. Rare Earths* **31**, 370–375 (2013). [https://doi.org/10.1016/S1002-0721\(12\)60288-9](https://doi.org/10.1016/S1002-0721(12)60288-9)
43. M.S. Bozgeyik, R.K. Katiyar, R.S. Katiyar, Improved magnetic properties of bismuth ferrite ceramics by La and Gd co-substitution. *J. Electroceramics* **40**, 247–256 (2018). <https://doi.org/10.1007/s10832-018-0126-1>
44. P. Kumar, N. Shankhwar, A. Srinivasan, M. Kar, Oxygen octahedra distortion induced structural and magnetic phase transitions in Bi_{1-x}Ca_xFe_{1-x}Mn_xO₃ ceramics. *J. Appl. Phys.* **117**, 194103 (2015). <https://doi.org/10.1063/1.4921433>
45. S. Duhalde, M.F. Vignolo, F. Golmar, C. Chilotte, C.E.R. Torres, L.A. Errico, A.F. Cabrera, M. Rentería, F.H. Sánchez, M. Weissmann, Appearance of room-temperature ferromagnetism in Cu-doped TiO_{2-δ} films. *Phys. Rev. B* **72**, 161313 (2005). <https://doi.org/10.1103/PhysRevB.72.161313>
46. C. Pascual-gonzalez, G. Schileo, S. Murakami, A. Khesro, D. Wang, I.M. Reaney, A. Feteira, BiFeO₃ ceramics Continuously controllable optical band gap in orthorhombic ferroelectric. *Appl. Phys. Lett.* **110**, 172902 (2017). <https://doi.org/10.1063/1.4982600>
47. S. Husain, A.O.A. Keelani, W. Khan, Influence of Mn substitution on morphological, thermal and optical properties of nanocrystalline GdFeO₃ orthoferrite. *Nano-Structures & Nano-Objects* **15**, 17–27 (2018). <https://doi.org/10.1016/j.nanoso.2018.03.002>
48. P. Uniyal, K.L. Yadav, Observation of the room temperature magnetoelectric effect in Dy doped BiFeO₃. *J. Phys. Condens. Matter* **21**, 10–13 (2009). <https://doi.org/10.1088/0953-8984/21/1/012205>

49. Y.P. Wang, L. Zhou, M.F. Zhang, X.Y. Chen, J.-M. Liu, Z.G. Liu, Room-temperature saturated ferroelectric polarization in BiFeO₃ ceramics synthesized by rapid liquid phase sintering. *Appl. Phys. Lett.* **84**, 1731–1733 (2004). <https://doi.org/10.1063/1.1667612>
50. J. Pal, S. Kumar, L. Singh, M. Singh, A. Singh, Study of the structural and magnetic phase-transitions and multiferroic properties in BiFeO₃-Ba_{0.95}Ca_{0.05}TiO₃ solid solutions. *Mater. Res. Bull.* **102**, 36–44 (2018). <https://doi.org/10.1016/j.materresbull.2018.02.012>
51. P.R. Vanga, R.V. Mangalaraja, M. Ashok, Effect of (Nd, Ni) co-doped on the multiferroic and photocatalytic properties of BiFeO₃. *Mater. Res. Bull.* **72**, 299–305 (2015). <https://doi.org/10.1016/j.materresbull.2015.08.015>
52. N. Kumar, A. Shukla, N. Kumar, R.N.P. Choudhary, A. Kumar, Structural, electrical, and multiferroic characteristics of lead-free multiferroic: Bi(Co_{0.5}Ti_{0.5})O₃-BiFeO₃ solid solution. *RSC Adv.* **8**, 36939–36950 (2018). <https://doi.org/10.1039/C8RA02306A>
53. A. Sagdeo, K. Gautam, P.R. Sagdeo, M.N. Singh, S.M. Gupta, A.K. Nigam, R. Rawat, A.K. Sinha, H. Ghosh, T. Ganguli, A. Chakrabarti, Large dielectric permittivity and possible correlation between magnetic and dielectric properties in bulk BaFeO_{3-δ}. *Appl. Phys. Lett.* **105**, 042906 (2014). <https://doi.org/10.1063/1.4892064>
54. C. Il Cheon, J.H. Choi, J.S. Kim, J. Zang, T. Frömling, J. Rödel, W. Jo, Role of (Bi_{1/2}K_{1/2})TiO₃ in the dielectric relaxations of BiFeO₃-(Bi_{1/2}K_{1/2})TiO₃ ceramics. *J. Appl. Phys.* **119**, 154101 (2016). <https://doi.org/10.1063/1.4946844>

Publisher's Note Springer Nature remains neutral with regard to jurisdictional claims in published maps and institutional affiliations.